ILASS Americas 28th Annual Conference on Liquid Atomization and Spray Systems, Dearborn, MI, May 2016

Numerical simulation of a shock wave impacting a droplet using the adaptive wavelet-collocation method

Zahra Hosseinzadeh-Nik[a], Mohamad Aslani[a], Mark Owkes[b], Jonathan D. Regele[a*]

[a]Department of Aerospace Engineering
Iowa State University
Ames, IA

[b]Department of Mechanical Engineering
Montana State University
Bozeman, MT

Abstract

Under startup conditions, supersonic combustors must atomize and ignite liquid fuel at hypersonic speeds. Little is known about fluid atomization in a supersonic cross flow experimentally and few methods exist to investigate the behavior numerically. In order to simulate this behavior an approach must be used that naturally accounts for the multiscale nature of the atomization process. In this work, a five equation interface-capturing scheme is developed to solve the compressible multi-component Navier-Stokes equations. The gas phase is modeled as an ideal gas and the liquid phase is modeled using a stiffened-gas equation of state. In order to account for the truly multiscale nature of this fluid behavior, the governing equations are solved using the highly efficient Parallel Adaptive Wavelet-Collocation Method (PAWCM). The PAWCM uses wavelets to dynamically adapt the grid used to represent the solution, which minimizes the overall computational cost and allows larger simulations to be performed. Shocks and interfaces are captured using a modified version of the hyperbolic solver developed specifically for the PAWCM. Surface tension is modeled using a continuous surface approach. One and two-dimensional simulations are used to demonstrate the method's capabilities.

* Corresponding Author

Introduction

The reliable atomization and ignition of liquid fuel injected into supersonic combustors is a significant limitation in SCRamjet development. Little is known about primary and secondary breakup processes in supersonic crossflows. A large body of literature exists that describes the breakup behavior of liquid droplets (secondary atomization) after being impacted by a shock wave to induce a strong shear[1]. However, most of the work uses shock waves that still induce subsonic post-shock velocities.

In shock tube experiments a droplet is impacted by a shock wave that passes over the droplet and causes minimal deformation during this interaction. The advantage of this approach is that a drop can be subjected to a step change in ambient flow that is nearly uniform over its surface[2]–[13]. An unequal pressure distribution forms around the droplet after the shock passes and deforms the initially spherical droplet. Interfacial tension and viscous forces resist this deformation and it is the competition between these resistive and pressure forces that determines the evolution of the droplet. Typical breakup modes include vibrational, bag, multimode, sheet-thinning, and catastrophic.

The use of direct numerical simulations has become more common in the last two decades to investigate droplet breakup and atomization behavior. Zaleski *et al.*[14] performed 2D water column simulations of the Navier-Stokes equations with constant density and viscosity. Igra and Takayama[15] showed experimentally that breakup behavior is similar between a 2D water column and a spherical droplet. Han and Tryggvason [16], [17] solved the axi-symmetric Navier-Stokes equations in order to simulate a spherical droplet fragmentation with a density ratio of 10. Transitional We numbers did not match experiments and it is thought that this may be because most experiments are conducted at much higher density ratios. Aalburg *et al.*[18] (expanded upon this work to simulate drop deformation at higher density ratios but did not have sufficient resolution to simulate breakup.

Quan and Schmidt[19] developed a 3D code with compressibility effects in ambient gas. Chang and Liou[20] developed a stratified flow model that can simulate the interaction of a shock wave with a liquid drop. Initial results indicate good agreement with experimental results of Theofanous *et al.*[13] at high Mach numbers. Khare *et al.*[21] used a volume of fluid method to perform full 3-D simulations using the incompressible multi-fluid Navier-Stokes equations and reproduced the transitional Weber numbers reasonably well.

Most of the studies on secondary atomization focus on the breakup of a spherical droplet from a shock wave (experimental) or impulsively started flow (numerical). While most of the numerical simulations of interfacial flows have been incompressible, there have been only a few studies[22]–[24] done in compressible flows. Other approaches neglect surface tension and analyze shock wave interactions with either bubbles[25]–[27] or the early stages of droplet deformation[28].

The breakup of droplets is a truly multiscale behavior and requires a multiscale approach. The Parallel Adaptive Wavelet-Collocation Method[29]–[31] is an intrinsically multiscale numerical approach that uses wavelets to determine which points are necessary to represent a solution within some *a priori* prescribed accuracy. In this work, a compressible multiphase interfacial flow methodology is developed within the PAWCM framework.

The paper is organized as follows. First the governing equations used to model the multiphase flow are described in detail. Second, the numerical method used to implement the system equations are described. Then some results demonstrating the method's capabilities are presented, followed by conclusions.

Multi-fluid compressible flow model

Multi-fluid/multi-component simulations are modeled using the quasi-conservative, volume fraction approach Navier-Stokes equations,

$$\frac{\partial(\rho_1\alpha_1)}{\partial t} + \nabla\cdot(\rho_1\alpha_1\boldsymbol{u}) = 0$$

$$\frac{\partial(\rho_2\alpha_2)}{\partial t} + \nabla\cdot(\rho_2\alpha_2\boldsymbol{u}) = 0$$

$$\frac{\partial(\rho\boldsymbol{u})}{\partial t} + \nabla\cdot(\rho\boldsymbol{u}\boldsymbol{u} + p\boldsymbol{I} - \boldsymbol{T}) = \boldsymbol{f}$$

$$\frac{\partial\rho e_t}{\partial t} + \nabla\cdot\left((\rho e_t + P\boldsymbol{I})\boldsymbol{u} - \boldsymbol{T}.\boldsymbol{u}\right) = \boldsymbol{f}\cdot\boldsymbol{u}$$

$$\frac{\partial\alpha_1}{\partial t} + \nabla\alpha_1 u = \alpha_1\nabla.u,$$

where ρ is the total density, $\boldsymbol{u}$ is the vector of velocity components, p is the pressure, e_t is the total energy, α is the volume fraction, $\boldsymbol{I}$ is the identity tensor and $\boldsymbol{T}$ is the stress tensor defined as,

$$\boldsymbol{T} = 2\mu\left(\frac{1}{2}(\nabla\boldsymbol{u} + (\nabla\boldsymbol{u})^T) - \frac{1}{3}(\nabla\cdot\boldsymbol{u})\boldsymbol{I}\right)$$

where μ is the shear stress. This coefficient is calculated using the mixture rule $\mu = \alpha_1\mu_1 + \alpha_2\mu_2$[27]. The current focus is on viscous effects and terms associated with thermal diffusion are ignored. Additionally μ_1 and μ_2 are modeled as constants so that μ is a function of composition only. Both assumptions, however, can be lifted, when appropriate terms are used to calculate temperature[32].

All equations are written in conservative form except the advection equation for the volume fraction. It has been shown that this equation is needed to calculate and preserve pressure equilibrium at the fluid interface and including the divergence term maintains $0 \leq \alpha_1 \leq 1$.

This set of equations is written for two fluids, but it is easily extendable to account for more than two fluids by adding a density and advection equation. Moreover, these equations conserve the mass of each fluid and the energy of the system and they do not generate spurious oscillations at the interface (necessary criteria for a multiphase simulation).

The system of equations is closed using the stiffened gas equation of state (EOS) to account for different phases in the flow,

$$p + \gamma\Pi^{\infty} = (\gamma - 1)\left(\rho e_t - \frac{1}{2}\rho \boldsymbol{u}\boldsymbol{u}\right),$$

where γ is the multicomponent ratio of specific heats and $\Pi^{\infty}(Pa)$ is the multicomponent fitting parameter for different components in the flow.

Following the mixture rules in the interface capturing method ($\rho_1\alpha_1 + \rho_2\alpha_2 = \rho, \alpha_1 + \alpha_2 = 1$), γ and Π^{∞} are found using the following:

$$\frac{1}{\gamma - 1} = \frac{\alpha_1}{\gamma_1 - 1} + \frac{1 - \alpha_1}{\gamma_2 - 1}$$

$$\frac{\gamma\Pi^{\infty}}{\gamma - 1} = \frac{\alpha_1\gamma_1\pi_1^{\infty}}{\gamma_1 - 1} + \frac{(1 - \alpha_1)\gamma_2\pi_2^{\infty}}{\gamma_2 - 1}$$

where values of γ and π^{∞} are listed in Table 1 for air, water, and Helium. The speed of sound is defined as $c = \sqrt{\gamma(p + \pi^{\infty})/\rho}$.

Any additional forces being applied to the fluid are contained in $\boldsymbol{f}$. In multiphase flows, one of the most important forces is the capillary force. Thus, the corresponding force and power terms are added to the system of equations using a continuum surface force model (CSF),

$$\boldsymbol{f} = -\sigma\kappa\nabla\alpha_1,$$

$$\boldsymbol{f}.\boldsymbol{u} = -\sigma\kappa\boldsymbol{u} \cdot \nabla\alpha_1,$$

where $\sigma(N/m)$ is the surface tension and κ is the curvature of the interface for the higher density fluid (in this case α_1). The curvature κ is calculated using

$$\kappa = \nabla \cdot \boldsymbol{n},$$

where $\boldsymbol{n} = \frac{\nabla\alpha_1}{|\nabla\alpha_1|}$ is the normal vector. Details on normal vector calculations are described in detail in the next section.

Finally, the above equations are non-dimensionalized using a reference density, speed of sound, and length scale. This introduces two non-dimensional parameters, namely the acoustic Reynolds and Weber numbers:

$$Re_a = \rho_0 c_0 l/\mu_0$$

$$We_a = \rho_0 c_0^2 l/\sigma.$$

Numerical Implementation

The Parallel Adaptive Wavelet Collocation Method (PAWCM), makes use of second generation wavelets to dynamically adapt the grid to localized structures in the flow in time and space[29]–[31]. This approach allows the solution to be approximated using a subset of the points that would normally be used with a uniform grid scheme. Dynamic domain partitioning is used for parallel computations and the method has been shown to scale well on up to 2048 processors[31].

In this paper, a second order finite difference discretization for the spatial terms are used along with a third order Total Variation Diminishing (TVD) Runge-Kutta (RK) time integration scheme. A modified version of the original hyperbolic solver developed for the PAWCM[33] that uses a TVD flux limiter to add artificial viscosity to the regions where a lower order flux is required. Therefore, for the tests that include sharp density and pressure jumps (e.g. shock waves), the order of accuracy drops to between first and second order in those regions. Similar to flux terms, the source terms are discretized in a consistent form.

Interface capturing model

For simplicity, both the shock and fluid interface are captured over several cells using an interface/shock

Fluid	$\rho[kg/m^3]$	γ	$\pi^{\infty}[GPa]$	$c[m/s]$
Air	1.205	1.4	0	343
Water	998	4.4	1	1450
Helium	0.166	1.67	0	1008

Table 1. Parameters used in stiffened gas EOS[27].

capturing approach. The diffusive nature of the numerical scheme requires the fluid interface to be steepened for certain variables. After the fluid evolution is solved for in physical time, the interface is steepened by iterating in false time τ.

The employed interface steepening technique uses a combination of interface and density sharpening to minimize the thickness of the numerically diffused interface. This approach uses a semi-conservative level set function where the volume fraction of the liquid phase indicates the interface. This function takes the values zero or one on either side of the interface with $\alpha_1 = 0.5$ indicating the actual interface location. The boundary between immiscible materials is modeled by the smooth variation of α_1 between these limits. Following the approach outlined by Shukla *et al*.[26], the interface function is steepened in false time using a compression step

$$\frac{d\alpha_1}{d\tau} = \boldsymbol{n} \cdot \nabla\big(\epsilon_h(\boldsymbol{n} \cdot \nabla\alpha_1) - \alpha_1\,(1-\alpha_1)\big),$$

where $\boldsymbol{n}$ is the normal vector and ϵ_h is a length-scale on the order of the grid spacing. In this equation the first term on the right hand side serves as a diffusion term to maintain nonlinear stability and the second term steepens the interface.

Since the density is a function of local flow conditions in compressible flows a separate steepening equation is required for each density equation. The approach outlined by Shukla *et al*.[26] is used to steepen the density. The compression step for the phase 1 density takes the form

$$\frac{d\alpha_1\rho_1}{d\tau} = H\boldsymbol{n} \cdot \big[\nabla\big(\epsilon_h.\nabla(\alpha_1\rho_1)\big) - (1-2\alpha_1)\nabla(\alpha_1\rho_1)\big]$$

The same approach is used for phase 2. The term *H* is a smoothed Heaviside function

$$H = \tanh\left[\left(\frac{(\alpha_1(1-\alpha_1)}{10^{-2}}\right)^2\right].$$

This function localizes the compression of density to the interface region.

The interface function and the density for each phase are steepened after each timestep. A single steepening iteration is used after each step in physical time. A false time CFL condition is established to calculate the false time step size $\Delta\tau = CFL_\tau \cdot h$, where h is the smallest grid size in the domain and CFL_τ is the steepening CFL number. Values for this parameter vary between 0.1 and 0.5 depending upon the desired steepness.

Normal vector calculation

Normal vectors are required to evaluate the right-hand side of the steepening equation and calculating the surface tension force. In both shock and interface capturing schemes, the representation of a sharp physical interface is most realistic if the interface thickness is minimized. This corresponds to taking ϵ_h as small as possible during the compression step. However, accurate computation of the gradients of the interface function, α_1, particularly those that define normal, are well-behaved only if α_1 is sufficiently resolved with the computational mesh. Otherwise, numerical artifacts appear and quickly disrupt the attractive properties of compression scheme. This is in contrast with the modeling objective of maintaining a sharp interface. In order to address this issue, Shukla et. al.[26] propose an auxiliary function

$$\psi = \frac{\alpha_1^\beta}{\alpha_1^\beta + (1-\alpha_1)^\beta}\,, \quad \beta < 1$$

that is more continuous across the fluid interface and provides gradients that contain less numerical noise. This function can be used to calculate the same normal vector values as would be calculated using α_1, but uses smoother gradients. The normal vector is then represented as

$$\boldsymbol{n} = \frac{\nabla\alpha_1}{|\nabla\alpha_1|} = \frac{\nabla\psi}{|\nabla\psi|}\,.$$

In this function a small value of β alleviates the problems associated the steep gradients of α_1 because the width of the hyperbolic tangent profile for ψ is $1/\beta$ times that of α_1. In this work $\beta = 0.1$ is usually sufficient to provide smooth and well-defined normal vectors.

An additional advantage of using the smoother function ψ to calculate the normal vectors instead of α_1 is that the curvature κ contains less noise after calculating a second derivative by using ψ. This approach eliminates the need to filter oscillations in the curvature retroactively.

Numerical Results

To show the robustness of the proposed method to solve compressible multiphase flows, 1-D and 2-D simulations have been performed. For brevity, only five test problems are contained here. Each problem has its own unique properties that assess the performance of the numerical method.

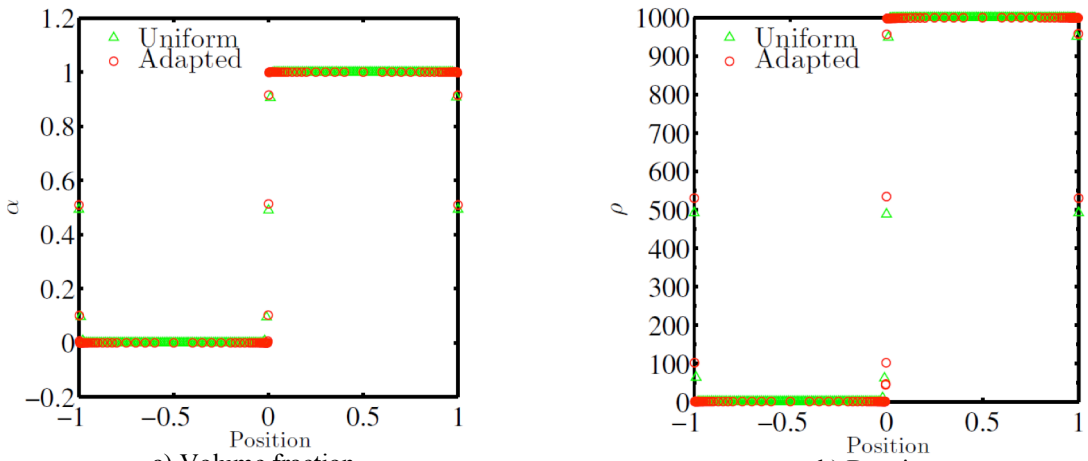

a) Volume fraction b) Density

Figure 1. Volume fraction (a) and density (b) for the 1-D advection problem.

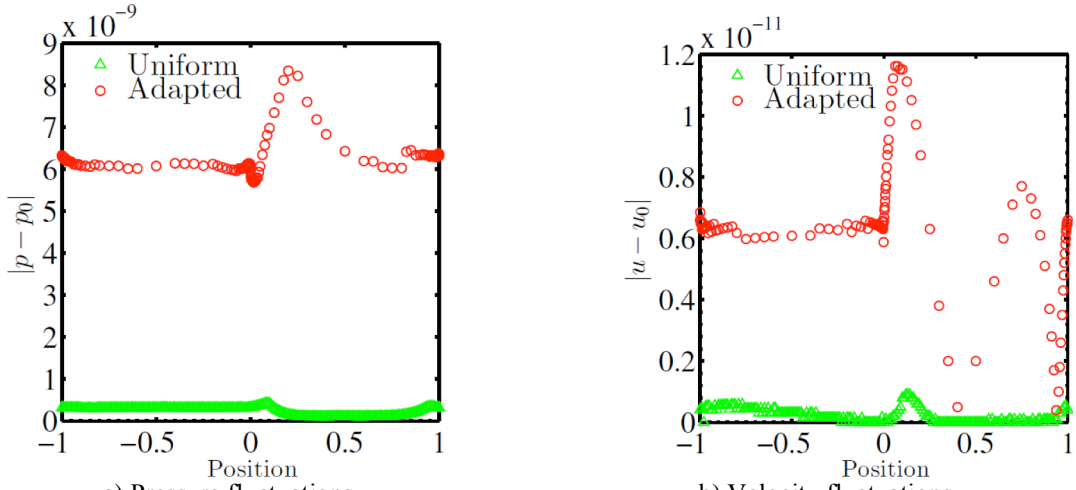

a) Pressure fluctuations b) Velocity fluctuations

Figure 2. Error in pressure and velocity fluctuations for the 1-D advection problem.

1D Advection of an isolated multiphase interface

The advection of an isolated water/air interface under atmospheric pressure in a periodic domain is a simple test that determines whether the numerical method produces any spurious oscillations at the fluid interface for pressure and velocity[27]. These oscillations, which appear initially in pressure terms ($O(10^{-6})$ to $O(10^{-1})$), may occur when the interface capturing method is not implemented correctly and or the conservative sharpening technique used is not consistent with the associated numerical implementation. No surface tension is used in this 1D simulation, but one iteration of steepening is applied with a $CFL_\tau = 0.25$.

The initial condition for the problem normalized by the density and speed of sound in water is[27]:

$$(\alpha_1\rho_1, \alpha_2\rho_2, u, P, \alpha_1) = \begin{cases} (1.204\times10^{-3}, 0, 0.01, 4.82\times10^{-5}, 1) & -1 \le x \le 0 \\ (0, 1, 0.01, 4.82\times10^{-5}, 0) & 0 \le x \le 1 \end{cases}$$

The solution is integrated in time with a CFL=0.5 for one period until $t = 20$. The volume fraction and density at the end of the simulation are shown in Fig. 1 for solutions on adaptive and uniform grids (200 cells). The figures show that only a minimal number of points are used across the interface and the adaptive method has the same solution with around half the points as the uniform grid. Also the method is able to handle high density ratios with minimal amounts of numerical diffusion.

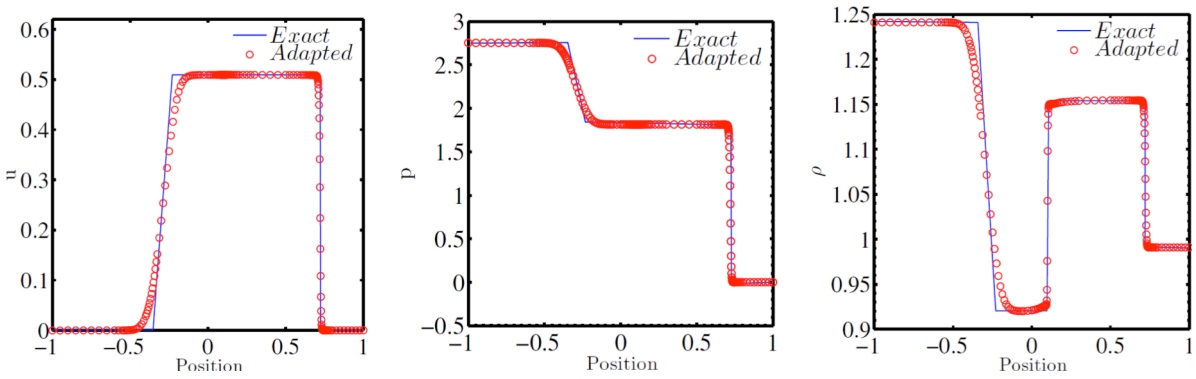

a) Velocity b) Pressure c) Density

Figure 3. Velocity (a), pressure (b), and density (c) distributions for the 1-D Riemann problem.

In order to demonstrate the magnitude of spurious oscillations at the interface, the error in pressure and velocity are plotted in Fig. 2. Both uniform and adaptive grids create minimal oscillations (error $\sim O(10^{-9})$), which confirms the ability of the method to minimize such errors, especially in an interface capturing method with high density ratios.

Gas-Liquid Riemann Problem

The gas liquid Riemann problem was originally used to model under water explosions. Since the problem incorporates two phases in a compressible set up, it is a good test problem for the stiffened gas equation of state. This problem contains no molecular viscosity.

Highly compressed air on the left is adjacent to water at atmospheric pressure on the right. The initial condition is given by[27]

$$(\alpha_1\rho_1, \alpha_2\rho_2, u, P, \alpha_1) = \begin{cases} (1.241,0,0,2.573,1) & -1 \le x < 0 \\ (0,0.991,0,3.059\times10^{-4},0) & 0 \le x \le 1 \end{cases}$$

The simulation is performed with a base grid of 20 points with 7 levels of refinement for an effective uniform grid resolution of 2,560 points. Of these 2,560 points, the solution is represented with around 100 points. The CFL number used for the time integration is 0.5 and the simulation is run until $t = 0.2$. Similar to the previous problem, a single step of steepening is performed in pseudo-time with a CFL_τ number of 0.25. Figure 3 compares the analytical solution with the numerical simulation for velocity, pressure and density. The results show that the method is able to predict the correct location of the transmitted and reflected shocks. As should be expected, the pressure and velocity are constant across the interface.

2D Advecting Water Column

The first two-dimensional test case is the advection of a water column. When a water column is advecting the spurious oscillations at the material interfaces can contaminate the fine flow features and have a negative impact on both the reliability and quality of computed solutions[27]. This can lead to interface deformation and mass loss. Therefore, the main challenge of this problem is shape preservation and mass conservation while moving. In this problem the rectangular computational domain is $\Omega = [-2.5, 2.5]\times[-2.5, 2.5]$. A water column of unit radius is placed in air with its center initially located at the origin. The rest of the initial condition for this problem, normalized by gas density and speed of sound, is

$$r = \sqrt{x^2 + y^2}$$

$$\alpha_1 = \frac{1}{2}\left(1 + \tanh\left(\frac{r-1}{\Delta}\right)\right)$$

$$(\alpha_1\rho_1, \alpha_2\rho_2, u, v, P) = \begin{cases} (10^3,0,0.5,,0.5,1) & r \le 1 \\ (0,1,0.5,0.5,1) & r > 1 \end{cases}$$

where phase 1 is water, $\alpha_1 = 1$, and phase 2 is air, $\alpha_1 = 0$. The maximum resolution grid spacing Δ is used in the initial condition to ensure that the initial profile always uses the same number of grid points across the interface. There is no molecular viscosity in this test case.

The solution is computed on an adaptive grid with two refinement levels to provide an effective grid of 160×160 points. Figure 4 demonstrates the interface function profile at (a) the initial condition, (b) after half a period, and (c) after 10 periods of advection. The water column moves diagonally in a periodic domain while the grids continuously adapt to the interface loca-

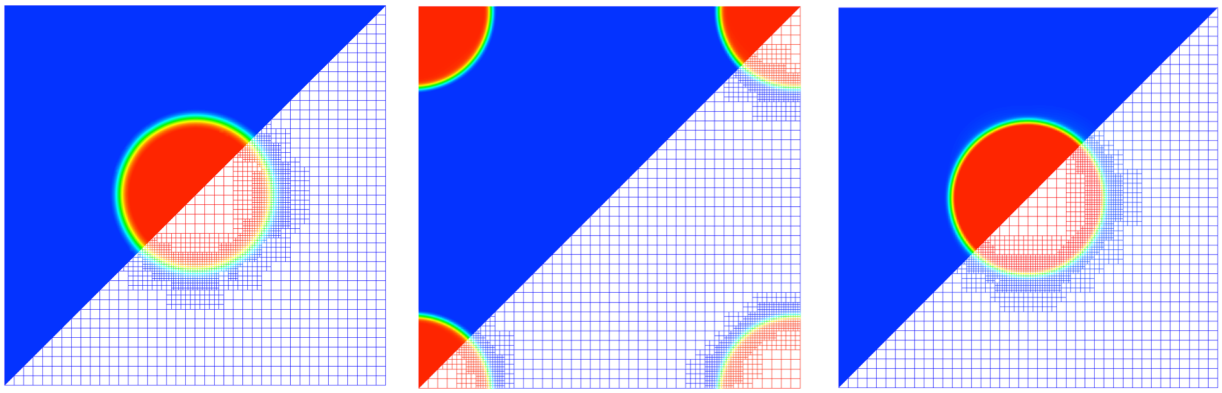

a) initial condition b) after half a period c) after 10 periods

Figure 4. Profile of interface function at a) the initial condition, b) after half a period, and c) after 10 periods.

tion. Figure 4(a) shows that the initial profile of the interface is smeared over several points. At the later times shown in Fig. 4(b) and (c), the compression scheme sharpens the interface and maintains a constant interface thickness of a few grid cells throughout the computations. Figure 4(c) also confirms that the method does not produce any noticeable oscillations near the interface.

A contour plot that illustrates the interface location ($\alpha_1 = 0.5$) for the initial condition and after 10 periods of advection is shown in Fig. 5. This shows that the interface size and shape is preserved and the mass is mostly conserved after several periods. The black circle after 10 periods has a smaller diameter than the initial red circle. This change is associated with the initial thickness of the interface being larger than the steady-state thickness that is maintained through a majority of the simulation.

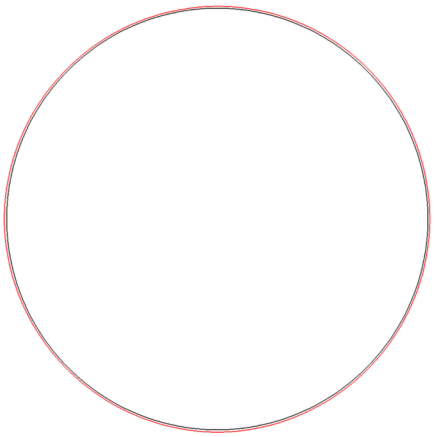

Figure 5. Comparison of the contour plot of interface location at initial condition (red line) and after 10 periods of advection (black line).

Shock water column interaction (no surface tension)

Now we consider the interaction of a strong planar shock wave ($M = 1.67$) interacting with a water column. The shock moves to the left and has an initial position of $x = 15$. The water column has an initial diameter $D = 2$ and is located at $x = 10$. The computational domain is $\Omega = [-20, 20]\times[-5, 5]$ and the equation of state parameters for water and air are given in Table. 1. The solution is computed on an adaptive grid with 2560×640 effective grid points.

Periodic boundary conditions are applied for the top and bottom boundaries. The left boundary is an outflow boundary. On the right boundary the post-shock condition is imposed. The Initial conditions are

$$r = \sqrt{(x-10)^2 + y^2}$$

$$\alpha_1 = \frac{1}{2}\left(1 + \tanh\left(\frac{r-1}{2\epsilon_h}\right)\right)$$

$$(\alpha_1\rho_1, \alpha_2\rho_2, u, v, P) = \begin{cases} (10^3\alpha_1, (1-\alpha_1), 0,0,0.714) & x < 10 \\ (0, 2.111, -0.892,0\ , 2.142) & x > 10 \end{cases}.$$

Figure 6 shows the early interaction of the shock wave with the water column. The results agree qualitatively with the results of Igra *et al.*[34]. The incident shock and the subsequent wave systems in the wake of the deforming cylinder are visualized using numerical Schlieren images of the gas phase density (defined $|\nabla\rho_2|$) in the top portion of each figure. The bottom of each figure shows the dynamically adaptive grid colored by pressure.

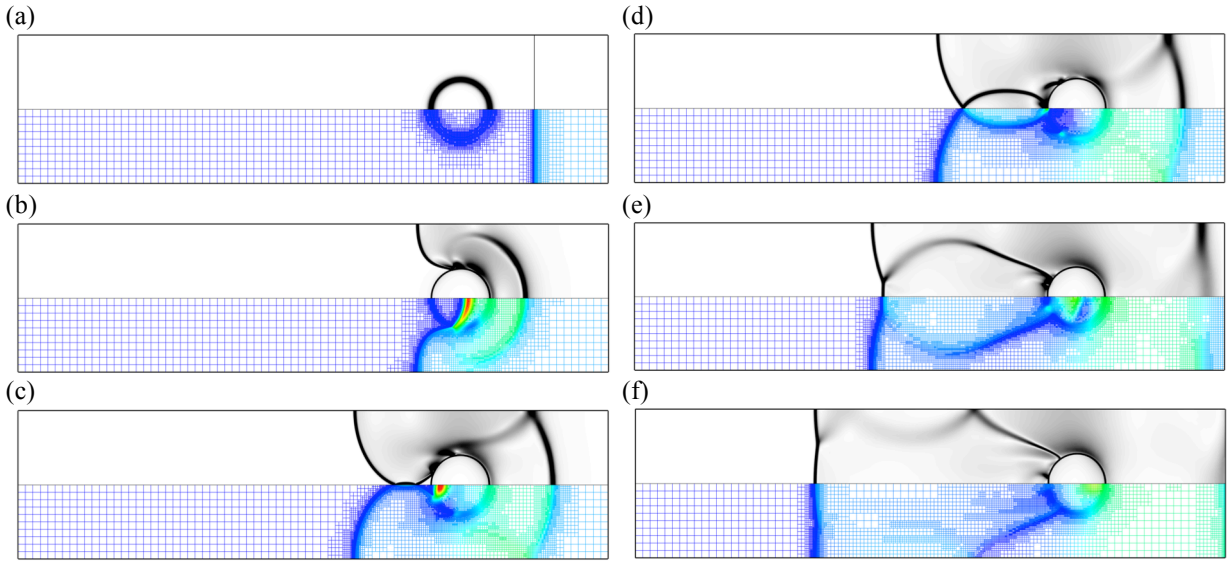

Figure 6. Numerical Schlieren images (top) and dynamic adaptive grids colored by pressure contours (bottom) of a shock wave passing through a liquid droplet at $t =$ (a) 0.00 (b) 4.8 (c) 7.5 (d) 9.00 (e) 12.00 (f) 14.80 (top to bottom, left to right).

Transmitted and reflected shocks are generated from the impact of the incident shock with the water column. The interaction of these waves with the interface leads to interfacial instabilities at the water-air interface and the wake structure behind the water column. There is a high-pressure region associated with the forward stagnation point, behind the reflected wave. A transition from a shock reflection to a Mach reflection happens at a critical angle behind the water column. This transition leads to maximum drag experienced by the column[28]. This phenomena has been reported in the literatures for both cylinders and spheres[34]. High pressure at the rear stagnation point is generated due to the convergent Mach stems behind the column.

It can be seen that the grid is localized to regions of the flow that have localized structures necessary of increased resolution. The results demonstrate that the dynamic grid adaptation used in the PAWCM approach makes the simulation of truly multiscale behavior such as this more computationally feasible for large-scale simulations.

Oscillating Ellipse

The last problem in this paper is an oscillating ellipse shaped water droplet with surface tension present. The initial pressure is uniform atmospheric pressure everywhere with zero velocity. The oscillation is due to the transfer between the potential energy of the interface and the kinetic energy of the fluid. The surface tension forces deform the shape into a neutral shape (preferably a circle), because the potential energy becomes a minimum and therefore the kinetic energy goes to a maximum in that phase ($t = T/4$). The inward acting momentum in the x-direction causes the ellipse to elongate in the y-direction ($t = T/2$). The same events move the ellipse interface back to the original shape ($t = T$). In order to illustrate the oscillation behavior, the globally integrated compressible kinetic energy

$$KE = \iint (\rho u^2 + \rho v^2) dA$$

is evaluated at each timestep. Figure 7 plots the KE over a single period T. It has been shown that the non-dimensional time period it takes for an ellipse ($x^2/a^2 + y^2/b^2 = 1$) to move back to the original shape after being disturbed by the surface tension forces is[22]:

$$T_{exact} = 2\pi \sqrt{\frac{We\left(1 + \frac{\rho_2}{\rho_1}\right) R^3}{6}}$$

where $R = \sqrt{ab}$. For $We = 1$, density ratio of 1000, and $Re = 100$ with $R = \sqrt{3/5 \times 5/3}$ for the ellipse, the period of oscillation becomes $T_{exact} = 81.15$. The simulation shows that this time is roughly about $T_{numerical} \approx 86.5$. It is suspected that the difference exists because secondary oscillation modes also exist. Further details on these other modes can be found in Ref. [22].

Figure 8 shows how the grid adapts to the droplets evolution with time. The high localization of the grid to

the surface makes the PAWCM method highly suitable to capturing the multiscale nature of atomization processes.

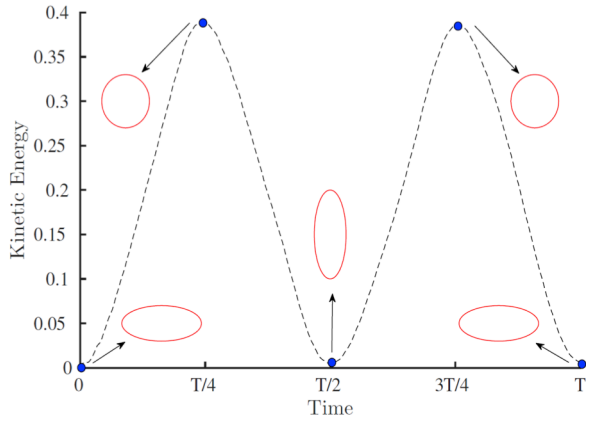

Figure 7. Kinetic energy versus time for a period of oscillation.

Conclusions

A compressible multiphase flow solver with surface tension is developed for the Parallel Adaptive Wavelet-Collocation Method. One-dimensional test problems show the ability to resolve both shock and interfaces over just a few points. Spurious oscillations in velocity and pressure are minimal across the interface. A two-dimensional test case for an advecting water column in air demonstrates the method's ability to maintain a steep fluid interface for long durations. An oscillating ellipse with surface tension was tested and the oscillation period matches the theoretical oscillation period reasonably well. For all cases, the grid dynamically adapts to the solution illustrating the power of the approach to handle large problems with a large range of scales.

Acknowledgements

This work is supported by Taitech, Inc. under subcontract TS15-16-02-004 (primary contract FA8650-14-D-2316).

References

1. Guildenbecher, D.R., López-Rivera, C. and Sojka, P.E., *Experiments in Fluids*, *46*(3):371-402 (2009).
2. Hinze, J.O., *AIChE Journal*, *1*(3):289-295 (1955).
3. Nicholls, J.A. and Ranger, A.A., *AIAA Journal*, *7*(2):285-290 (1969).
4. Gel'Fand, B.E., Gubin, S.A., Kogarko, S.M. and Komar, S.P., *J. eng. physics and thermophysics*, *25*(3):1140-1142 (1973).
5. Wierzba, A. and Takayama, K., *AIAA journal*, *26*(11):1329-1335 (1988).
6. Hsiang, L.P. and Faeth, G.M., *Int. J. Multiphase Flow*, *18*(5):635-652 (1992).
7. Hsiang, L.P. and Faeth, G.M., *Int. J. Multiphase Flow*, *19*(5):721-735 (1993).
8. Hsiang, L.P. and Faeth, G.M., *Int. J. Multiphase Flow*, *21*(4):545-560 (1995).
9. Chou, W.H., Hsiang, L.P. and Faeth, G.M., *Int. J. Multiphase Flow*, *23*(4):651-669 (1997).
10. Joseph, D.D., Belanger, J. and Beavers, G.S., *Int. J. Multiphase Flow*, *25*(6):1263-1303 (1999).
11. Joseph, D.D., Beavers, G.S. and Funada, T., *J. Fluid Mech.*, *453*:109-132 (2002).

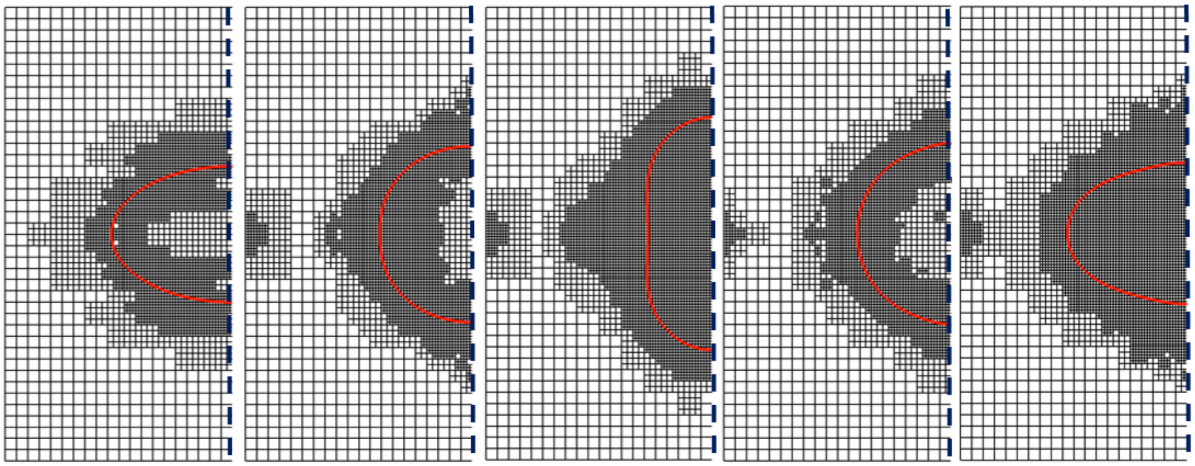

Figure 8. Grid adaptation during one period for the oscillating ellipse problem with 5 levels of adaptation.

12. Dai, Z. and Faeth, G.M., *Int. J. Multiphase Flow*, *27*(2):217-236 (2001).
13. Theofanous, T.G., Li, G.J. and Dinh, T.N., *J. fluids eng.*, *126*(4):516-527 (2004).
14. Zaleski, S., Li, J. and Succi, S., *Physical review letters*, *75*(2):244 (1995).
15. Igra, D. and Takayama, K., *Shock Waves*, *11*(3):219-228 (2001).
16. Han, J. and Tryggvason, G., I., *Physics of Fluids*, *11*(12):3650-3667 (1999).
17. Han, J. and Tryggvason, G., *Physics of Fluids*, *13*(6):1554-1565 (2001).
18. Aalburg, C., Leer, B.V. and Faeth, G.M., *AIAA journal*, *41*(12):2371-2378 (2003).
19. Quan, S. and Schmidt, D.P., *Physics of Fluids*, *18*(10):102-103 (2006).
20. Chang, C.H. and Liou, M.S., *J. of Computational Physics*, *225*(1):840-873 (2007).
21. P. Khare, D. Ma, X. Chen, and V. Yang, 12th *ICLASS, Heidelberg, Ger. (*2012).
22. Perigaud, G. and Saurel, R., *J. of Computational Physics*, *209*(1):139-178 (2005).
23. Braconnier, B. and Nkonga, B., *J. of Computat. Physics*, *228*(16):5722-5739 (2009).
24. Shukla, R.K., *Journal of Computational Physics*, *276*, pp.508-540 (2014).
25. Johnsen, E. and Colonius, T., *Proc. Sixth Int. Symp. on Cavitation, Wageningen, The Netherlands, September* (2006).
26. Shukla, R.K., Pantano, C. and Freund, J.B., 2010. *Journal of Computational Physics*, *229*(19):7411-7439 (2010).
27. Coralic, V. and Colonius, T., *J. computational physics*, *274*:95-121 (2014).
28. Meng, J.C. and Colonius, T., *Shock Waves*, *25*(4):399-414 (2015).
29. Vasilyev, O.V. and Bowman, C., *J. Comput. Physics*, *165*(2):660-693 (2000).
30. Vasilyev, O.V., *Int. J. of Computational Fluid Dynamics*, *17*(2):151-168 (2003).
31. Nejadmalayeri, A., Vezolainen, A., Brown-Dymkoski, E. and Vasilyev, O.V., *J. Comput. Physics*, *298*:237-253 (2015).
32. Beig, S.A. and Johnsen, E., *J.Comput. Physics*, *302*:548-566 (2015).
33. Regele, J.D. and Vasilyev, O.V., *Int. J. Comput. Fluid Dyn.*, *23*(7):503-518 (2009).
34. Tanno, H., Itoh, K., Saito, T., Abe, A. and Takayama, K., *Shock Waves*, *13*(3):191-200 (2003).